

Efficiently Calibrating Cable-Driven Surgical Robots With RGBD Sensing, Temporal Windowing, and Linear and Recurrent Neural Network Compensation

Minho Hwang¹, Brijen Thananjeyan¹, Samuel Paradis¹, Daniel Seita¹, Jeffrey Ichnowski¹,
Danyal Fer², Thomas Low³, and Ken Goldberg¹

Abstract—Automation of surgical subtasks using cable-driven robotic surgical assistants (RSAs) such as Intuitive Surgical’s da Vinci Research Kit (dVRK) is challenging due to imprecision in control from cable-related effects such as backlash, stretch, and hysteresis. We propose a novel approach to efficiently calibrate a dVRK by placing a 3D printed fiducial coordinate frame on the arm and end-effector that is tracked using RGBD sensing. To measure the coupling effects between joints and history-dependent effects, we analyze data from sampled trajectories and consider 13 modeling approaches using LSTM recurrent neural networks and linear models with varying temporal window length to provide corrective feedback. With the proposed method, data collection takes 31 minutes to produce 1800 samples and model training takes less than a minute. Results suggest that the resulting model can reduce the mean tracking error of the physical robot from 2.96 mm to 0.65 mm on a test set of reference trajectories. We evaluate the model by executing open-loop trajectories of the FLS peg transfer surgeon training task. Results suggest that the best approach increases success rate from 39.4 % to 96.7 % comparable to the performance of an expert surgical resident. Supplementary material, including 3D-printable models, is available at <https://sites.google.com/berkeley.edu/surgical-calibration>

I. INTRODUCTION

Accurate control of cable-driven surgical robots such as the da Vinci Research Kit [10] is challenging due to cable-related effects such as backlash, hysteresis, and cable tension [15], [5]. These effects result in errors in the robot’s odometry, because the encoders tracking the joint positions are frequently located near the motors but far from the joints themselves. Due to the high accuracy required to perform surgical subtasks, automation of robot-assisted surgery can be very difficult [9], [32], and may require slow and tedious manual calibration [9], [25]. In current practical applications for robot surgery, human surgeons compensate for these inaccuracies.

In this paper, we present a method to efficiently calibrate a dVRK by placing 3-D printed fiducials on the end effector and arm (see Fig. 1), designing an estimation algorithm to measure the robot’s ground truth joint configuration, and training a controller that compensates for history-dependent cabling effects. We also present empirical analysis of these effects.

¹AUTOLAB at the University of California, Berkeley, USA. <http://autolab.berkeley.edu/>

²UC San Francisco East Bay, USA.

³SRI International, USA.

Correspondence to: Minho Hwang, gkgkgk1215@berkeley.edu

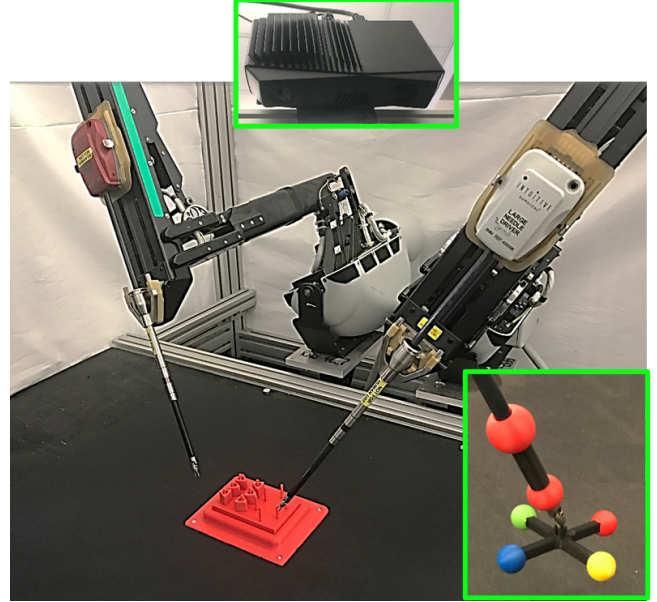


Fig. 1: da Vinci Research Kit (dVRK) with 3D-printed spherical fiducials that facilitate tracking of true location of the six joints. A Zivid OnePlus RGBD camera is mounted 0.9 meters above the workspace (top).

Prior work has studied learning to compensate joint estimation errors by considering current observations of robot state [13], [25], [20]. To compensate for history-dependent effects such as hysteresis and backlash, we explore temporal awareness by incorporating a horizon of observations. We investigate design choices such as: temporal window size, linear modeling vs. deep learning, forward vs. inverse system identification, and usage of prior model outputs as current inputs. The best approach is a recurrent neural network modeling the forward dynamics with a temporal window of 4, which is able to reduce the mean-squared joint error from 0.039 to 0.00061 on a held out test set of random trajectory data. As the model fits data for a specific instrument to model its specific cabling effects, the calibration procedure needs to be efficient. With the proposed method, data collection takes 31 minutes to produce 1800 samples and model training takes less than a minute.

We integrate the compensatory model into the robot’s control loop, and run automated trials of a variant of peg transfer using open loop trajectories. The peg transfer task is part of the Fundamentals of Laparoscopic Surgery and is a standard training task for surgeons that requires high precision motions and dexterity to perform. Prior work on automating

the task either used hand-tuned calibration procedures [9] or visual servoing [21] to compensate for robot inaccuracies. Experiments suggest that the new calibration method is able to increase the per-block transfer success rate from 39.4 % to 96.7 % without visual servoing.

This work makes the following contributions: (1) a low-cost hardware fiducial design used with RGBD to track ground-truth joint positions of the dVRK, (2) experiments suggesting that the wrist joints are the main source of state estimation errors, (3) correction of robot joint position estimation errors using an LSTM recurrent neural network that considers history of observations and predictions, (4) robot experiments suggesting that the corrective model can significantly increase the accuracy and precision of open-loop trajectories in a challenging peg transfer task.

II. RELATED WORK

Surgical robots are routinely used to perform operations in hospitals worldwide through teleoperation with complete control by human surgeons, and no procedures in clinical settings today include autonomous subtasks. In research settings, several groups have demonstrated results in automating surgical subtasks, such as suturing [23], [26], [19], [22], cutting gauze [29], [27], smoothing fabrics [24], identifying tumors via palpation [14], [4], performing debridement [11], [16], tying knots [31], inserting and extracting surgical needles [2], [28], [33], and transferring blocks in the peg transfer task [21], [9].

These surgical tasks often require positional accuracies bounded within 2-3mm, which is difficult to obtain with cable-driven Robot Surgical Assistants such as the da Vinci [10], the Raven II [6], and especially flexible surgical robots [8], [12], as they are known to suffer from cable stretch and tension, backlash, and hysteresis. Research groups have taken various approaches to compensating for these inaccuracies, such as by using Unscented Kalman Filters to improve joint angle estimation [5] estimating cable stretch and friction [15], or directly learning offsets to correct for robot end-effector positions and orientations [17], [13], [25].

In among the most relevant prior work, Peng et al. [20] recently reported a data-driven calibration method for the Raven II [6]. They use three spheres and four RGB cameras to estimate the position of the Raven II end-effector. They collect a labeled dataset of 49,407 positions and train a neural network to predict the robot's 3D position to within 1mm accuracy on an offline test set. In contrast to their work, we consider the problem of estimating the joint configuration, which can be incorporated more directly in collision checking, and we also learn to predict the commanded input given a history and desired joint angle. Additionally, we use both RGB and depth sensing to track the sphere fiducials and consider historical motions in the estimation of joint angles, which enable compensation for hysteresis and backlash. Furthermore, we design practical controllers using these models and benchmark the result of applying the proposed calibration procedure on a challenging peg transfer task.

III. PROBLEM DEFINITION

Let \mathbf{q}_p be the specification of the degrees of freedom, or *configuration*, of the da Vinci Research Kit. Let $\mathcal{C}_p \subset \mathbb{R}^6$ be the set of all possible configurations, thus $\mathbf{q}_p \in \mathcal{C}_p$. Let $\mathbf{q}_c \in \mathcal{C}_c$ be the robot's commanded configuration, where $\mathcal{C}_c \subset \mathbb{R}^6$ and is equivalent to the joint configurations measurable by the robot's encoders. Note that this differs from \mathbf{q}_p , because the encoders are located at the motors and away from the joints, which can result in a mismatch between the joint position measured by the encoders and the true joint positions due to cabling effects. We use subscripts to index specific joints in vectors, e.g., $\mathbf{q}_p^\top = [\mathbf{q}_{p,1} \ \dots \ \mathbf{q}_{p,6}]$. See Fig. 3 for visualization of joints $\mathbf{q}_1, \dots, \mathbf{q}_6$, where we suppress the p or c subscripts when the distinction is not needed. Let $\tau_t = (\mathbf{q}_c^{(0)}, \dots, \mathbf{q}_c^{(t-1)}) \in \mathcal{T}$ encode the prior trajectory information of the robot up to time t . The goal of this paper is to compute two functions:

$$\begin{aligned} f : \mathcal{C}_c \times \mathcal{T} &\rightarrow \mathcal{C}_p \\ g : \mathcal{C}_p \times \mathcal{T} &\rightarrow \mathcal{C}_c, \end{aligned}$$

where $f(\cdot)$ maps the current command at time t and prior state information to the current physical state of the arm, and $g(\cdot)$ maps the current physical state of the arm and its history to the command that was executed at time t . The intent for $f(\cdot)$ is to determine the physical configuration of a robot given the commands that one sent to it. The intent for $g(\cdot)$ is to derive commands to move the robot to a desired physical configuration. We also explore using f for this purpose by approximately inverting it to obtain the input control that produces a desired output position. At execution time, we would like to use the controller derived from $g(\cdot)$ to track a reference trajectory of target waypoints $(\mathbf{q}_d^{(t)})_{t=0}^T$ where $\mathbf{q}_d^{(t)} \in \mathcal{C}_p$. We also consider control generation via the forward model f by approximately inverting it for a desired output waypoint. Observe that these functions are history-dependent inverses of each other, i.e., $g(f(\mathbf{q}_c^{(t)}, \tau_t), \tau_t) = \mathbf{q}_c^{(t)}$ and $f(g(\mathbf{q}_p^{(t)}, \tau_t), \tau_t) = \mathbf{q}_p^{(t)}$.

Complicating this objective is a significant sub-problem of computing \mathbf{q}_p at any moment in time. While \mathbf{q}_c can be readily determined by reading the encoders associated with each joint, \mathbf{q}_p must be determined by other means. Additionally, because enumerating the set of possible trajectories is intractable, parametric approximations $f_\theta \approx f$ and $g_\phi \approx g$ must be estimated from a finite sequence of samples $\mathcal{D} = \left((\mathbf{q}_c^{(t)}, \mathbf{q}_p^{(t)}) \right)_{t=0}^N$.

IV. METHOD

In this section, we describe the methods to learn f_θ and g_ϕ from data and then use the learned functions to accurately control the robot. We start by sending a sequence of \mathbf{q}_c and tracking the physical trajectories of fiducial markers attached to the robot. We then convert the marker's positions to \mathbf{q}_p using kinematic equations. After collecting several of datasets of \mathbf{q}_c and its resulting \mathbf{q}_p , we then train 15 models and implement a controller.

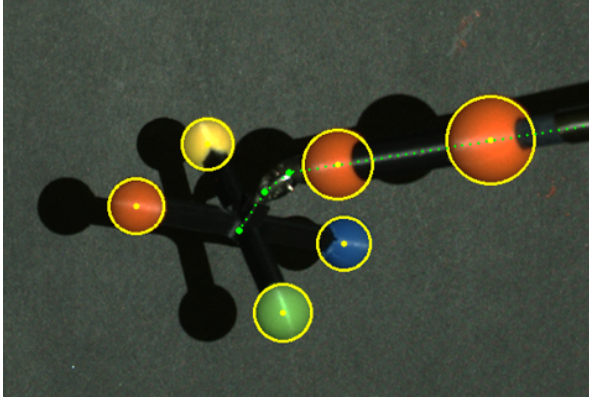


Fig. 2: Sphere fiducials to estimate the pose of the end effector. We place two spheres on the shaft to obtain wrist position and four on the cross-shaped reference frame to find the orientation of the jaw. Yellow circles and dots indicate the detected spheres and its center locations. The green dotted lines show a skeleton of the estimated tool posture.

A. Sphere Position Detection Algorithm

Peng et al. [20] use 4 RGB cameras to detect positions of 3 spheres on the end-effector, requiring 16 marker points to calibrate the cameras. They use functions from OpenCV to implement edge detection, color segmentation, and Hough circle detection.

In this work, to estimate \mathbf{q}_p , we use an RGBD camera to track a fixture of colored spheres attached to the end effector (Fig. 2). By masking depth and color ranges, we more robustly detect each of the spheres regardless of image background. We attach 4 spheres on the end-effector to ensure at least three are visible in case of occlusions. We mount 2 additional spheres on the tool shaft to decouple the first three joints from the last three and therefore to identify potential coupling effects among joints. These are designed and placed where they cannot overlap in the camera image within the working range of joints. We implement image segmentation using functions from OpenCV [1]. With the n 3D-points $(x_i, y_i, z_i)_{i=0}^{n-1}$ corresponding to each segmented sphere obtained from the depth image, we formulate the following linear regression $\mathbf{A}\mathbf{c} = \mathbf{b}$:

$$\underbrace{\begin{bmatrix} x_0 & y_0 & z_0 & 1 \\ \vdots & \vdots & \vdots & \vdots \\ x_{n-1} & y_{n-1} & z_{n-1} & 1 \end{bmatrix}}_{\mathbf{A} \in \mathbb{R}^{n \times 4}} \underbrace{\begin{bmatrix} \mathbf{c}_0 \\ \mathbf{c}_1 \\ \mathbf{c}_2 \\ \mathbf{c}_3 \end{bmatrix}}_{\mathbf{c} \in \mathbb{R}^{4 \times 1}} = \underbrace{\begin{bmatrix} x_0^2 + y_0^2 + z_0^2 \\ \vdots \\ x_{n-1}^2 + y_{n-1}^2 + z_{n-1}^2 \end{bmatrix}}_{\mathbf{b} \in \mathbb{R}^{n \times 1}}$$

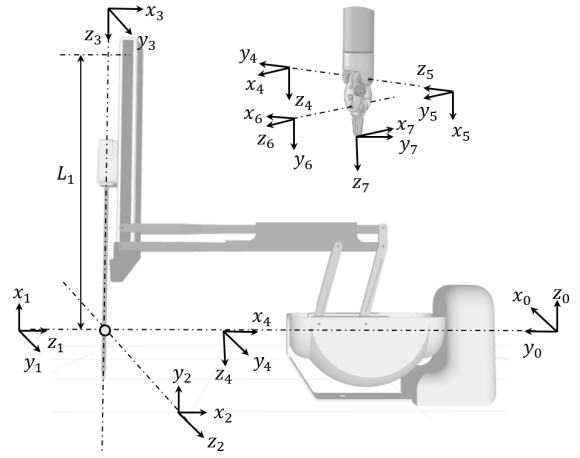
to obtain \mathbf{c} , and thus the center position of each sphere b :

$$\mathbf{p}_b = [x_b \ y_b \ z_b]^\top = \frac{1}{2} [\mathbf{c}_0 \ \mathbf{c}_1 \ \mathbf{c}_2]^\top \quad (\text{IV.1})$$

with its radius as $r_b = \sqrt{x_b^2 + y_b^2 + z_b^2}$.

B. Configuration Estimation of Surgical Tool

As shown in Fig. 2, the tool shaft has two spheres on it to obtain its wrist position, which excludes the last three joint angles of the surgical tool in the calculation. We attach four spheres to the edge of the cross-shaped reference frame to find the orientation of the jaw. One of the four spheres



Frame	Joint Name	a	α	d	θ
1	Arm Yaw	0	$\pi/2$	0	$q_1 + \pi/2$
2	Arm Pitch	0	$-\pi/2$	0	$q_2 + \pi/2$
3	Arm Insertion	0	$\pi/2$	$q_3 - L_1$	0
4	Tool Roll	0	0	L_{tool}	q_4
5	Tool Pitch	0	$-\pi/2$	0	$q_5 + \pi/2$
6	Tool Yaw	-	$-\pi/2$	0	$q_6 + \pi/2$
7	End Effector	0	$-\pi/2$	-	0
8	Match to Base	0	π	0	π

Fig. 3: Coordinate frames are assigned following the modified Denavit-Hartenberg convention. For $i \in \{1, \dots, 6\}$, the illustrated coordinate frame (x_i, y_i, z_i) above corresponds to \mathbf{q}_i as used in the text. We use the kinematic equations to estimate the tool pose described in Section IV-B.

is redundant to ensure that occlusion from the camera view does not hinder estimating physical joint angles.

From the kinematic equations in Fig. 3, we can obtain the joint angles $\mathbf{q}_{p,1}$, $\mathbf{q}_{p,2}$, and $\mathbf{q}_{p,3}$ in terms of the position of the wrist joint 0p_5 , which is the measured position from extending two positions of the spheres on the shaft, as follows:

$${}^0p_5 = {}^0T \cdot {}^5p_{org}$$

$$\begin{bmatrix} {}^0x_5 \\ {}^0y_5 \\ {}^0z_5 \end{bmatrix} = \begin{bmatrix} \cos(\mathbf{q}_{p,2}) \cdot \sin(\mathbf{q}_{p,1}) \cdot (L_t - L_1 + \mathbf{q}_{p,3}) \\ -\sin(\mathbf{q}_{p,2}) \cdot (L_{\text{tool}} - L_1 + \mathbf{q}_{p,3}) \\ -\cos(\mathbf{q}_{p,1}) \cdot \cos(\mathbf{q}_{p,2}) \cdot (L_t - L_1 + \mathbf{q}_{p,3}) \end{bmatrix} \quad (\text{IV.2})$$

$$\begin{bmatrix} \mathbf{q}_{p,1} \\ \mathbf{q}_{p,2} \\ \mathbf{q}_{p,3} \end{bmatrix} = \begin{bmatrix} \arctan(x/z) \\ \arctan(-y/\sqrt{x^2 + z^2}) \\ \arctan(\sqrt{x^2 + y^2 + z^2} + L_1 - L_2) \end{bmatrix}, \quad (\text{IV.3})$$

where ${}^5p_{org}$ is the origin of the 5th coordinate frame and L_t is the length of the surgical tool. The last three joint angles, \mathbf{q}_4 , \mathbf{q}_5 , and \mathbf{q}_6 , can be computed from the rotation matrix of the fiducial markers on the jaw as follows:

$${}^3_8R = ({}^0_3R)^{-1} \cdot {}^0_{\text{marker}}R = \begin{bmatrix} r_{11} & r_{12} & r_{13} \\ r_{21} & r_{22} & r_{23} \\ r_{31} & r_{32} & r_{33} \end{bmatrix} \quad (\text{IV.4})$$

$$\begin{bmatrix} \mathbf{q}_{p,4} \\ \mathbf{q}_{p,5} \\ \mathbf{q}_{p,6} \end{bmatrix} = \begin{bmatrix} \arctan(-r_{22}/r_{12}) \\ \arctan(-r_{31}/r_{33}) \\ \arctan(r_{32}/\sqrt{r_{31}^2 + r_{33}^2}) \end{bmatrix}, \quad (\text{IV.5})$$

giving us the full procedure for getting all six joints $\mathbf{q}_p^\top = [\mathbf{q}_{p,1} \ \dots \ \mathbf{q}_{p,6}]$.

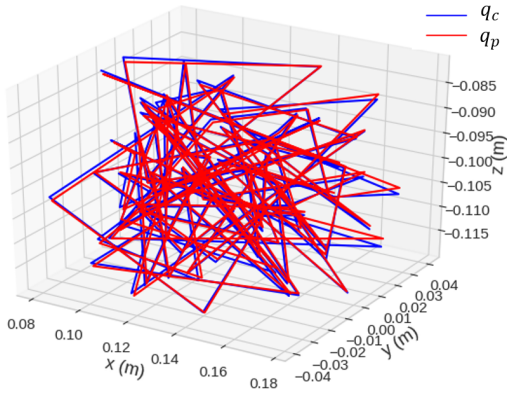


Fig. 4: **Random Trajectories:** We collect a dataset $\mathcal{D}_{\text{rand}}$ of randomly sampled configurations of the robot throughout its workspace for training. We collect both the commanded (desired) joint angles and the actual physical joint angles.

C. Data Collection

We generate a training dataset containing pairs of desired and actual joint angles of the robot. In the data collection process, we randomly sample configurations of the robot throughout its workspace of 100 mm x 80 mm x 40 mm. Then, we command the robot to replay the executed trajectory with the sphere fixture attached. This enables us to collect ground truth information for trajectories that are executed during a task. During the process, we collect the actual \mathbf{q}_p and commanded joint angles \mathbf{q}_c to compile a dataset \mathcal{D} :

$$\mathcal{D} = \left((\mathbf{q}_c^{(t)}, \mathbf{q}_p^{(t)}) \right)_{t=1}^N. \quad (\text{IV.6})$$

We collect the following datasets:

- Random motions ($\mathcal{D}_{\text{rand}}$): This dataset consists of random sampled configurations of the robot (Fig. 4). It took 66 minutes to collect 4000 datapoints.
- Pick and place motions ($\mathcal{D}_{\text{pick}}$): This dataset consists of horizontal motions where the z coordinate of the end effector is fixed and vertical motions where only the z coordinate is varied (Fig. 5). It took 31 minutes to collect 1800 datapoints.

D. Error Identification

We conduct a preliminary study to identify the characteristics of error and the coupling effect among joints. We sub-sample a portion of the dataset from Section IV-C with $N = 270$. We then replay the trajectory but keep the first 3 joint angles fixed. Fig. 6 presents the desired and measured trajectory of each joint angle in both cases. We notice that the three joints of the robot arm, $\mathbf{q}_{p,1}$, $\mathbf{q}_{p,2}$, and $\mathbf{q}_{p,3}$, rarely contribute to the error compared to the last 3 joints, since the root mean square errors, RMSE, are 0.001 rad, 0.001 rad, and 0.255 mm for each. It is noteworthy that the three joints of the surgical tool, $\mathbf{q}_{p,4}$, $\mathbf{q}_{p,5}$, and $\mathbf{q}_{p,6}$, are repeatable and not affected by the arm joints. In addition, results suggest that the last two joints are closely coupled, since $\mathbf{q}_{p,5}$ synchronously moved with $\mathbf{q}_{p,6}$ even though it was commanded to be stationary, and vice versa (Fig. 6).

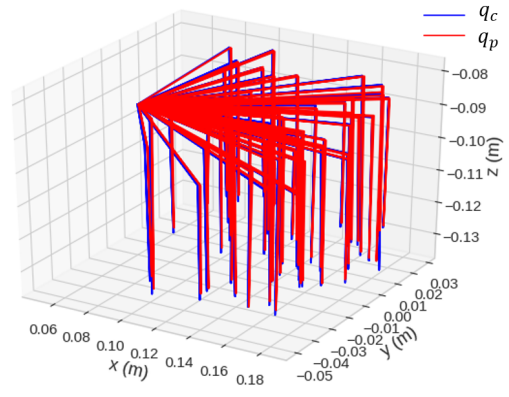


Fig. 5: **Pick and Place Trajectories:** We collect a dataset $\mathcal{D}_{\text{pick}}$ of pick and place motions in the workspace. We use these motions to train a controller specifically optimized for the peg transfer task (Section V-D).

Algorithm 1 Control Optimization Algorithm

Require: Target position $\mathbf{q}_d^{(t)}$, state estimator f_θ , number of iterations M , learning rate α

- 1: $\mathbf{q}_c^{(t)} \leftarrow \mathbf{q}_d^{(t)}$
 - 2: **for** $j \in \{1, \dots, M\}$ **do**
 - 3: $\Delta_j \leftarrow \mathbf{q}_d^{(t)} - f_\theta(\mathbf{q}_c^{(t)}; \tau_t)$
 - 4: $\mathbf{q}_c^{(t)} \leftarrow \mathbf{q}_c^{(t)} + \alpha \Delta_j$
 - 5: **return** $\mathbf{q}_c^{(t)}$
-

E. State Estimation Without Attached Fixtures

To estimate \mathbf{q}_p without the fixtures attached, we propose training a function approximator $f_\theta : \mathcal{C}_c \times \mathcal{T} \rightarrow \mathcal{C}_p$, such that $f_\theta(\mathbf{q}_c^{(t)}, \tau_t) = \hat{\mathbf{q}}_p^{(t)} \approx \mathbf{q}_p^{(t)}$.

We also train an inverse model $g_\varphi(\mathbf{q}_p^{(t)}, \tau_t) = \hat{\mathbf{q}}_c^{(t)} \approx \mathbf{q}_c^{(t)}$. In this notation, the subscripts θ and φ represents the parameters of the learned model. In Section V-A, we investigate training f_θ and g_φ using linear regression and deep neural networks of differing architectures and prior state inputs.

F. Controller Design

Once we train function approximators, we would like to apply them accurately control the robot while compensating for the robot's cabling effects. Since the learned inverse model g_φ estimates commands, it can be used directly for this purpose. However, as we show in Section V, in some cases we can more accurately position the robot using the forward model as a basis for a controller. This controller takes as input the target joint position $\mathbf{q}_d^{(t)}$ and computes joint position command $\mathbf{q}_c^{(t)}$ to get the robot to that position. The algorithm for this controller (Alg. 1) iteratively refines the command based on error with respect to the target position. The algorithm evaluates the forward dynamics f_θ for an input command to obtain an estimate of the next configuration ($f_\theta(\mathbf{q}_c^{(t)}; \tau_t)$). Then, the algorithm guides the command to compensate for the error with respect to the target position. This process is repeated for M iterations.

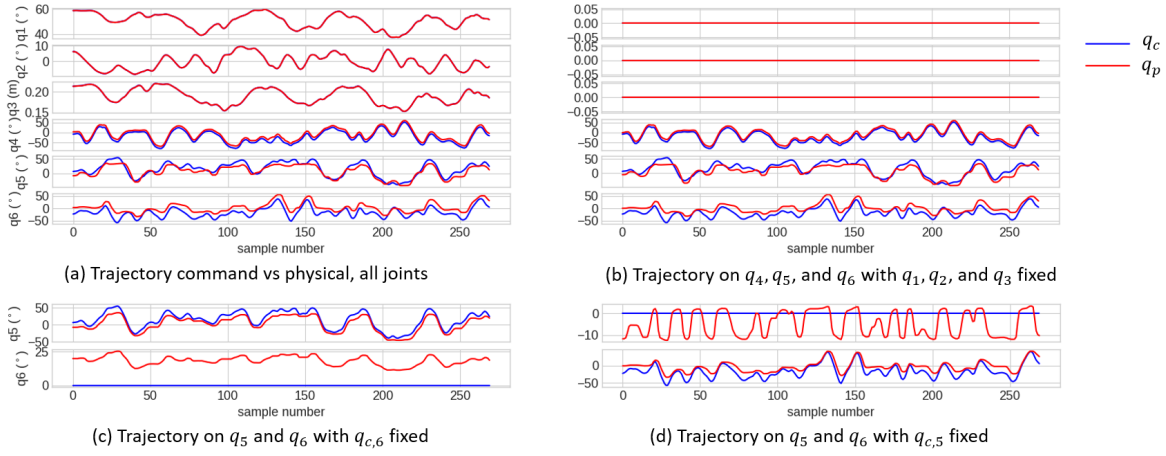


Fig. 6: **Top row:** We observe that the tool joint angles $\mathbf{q}_{p,4}$, $\mathbf{q}_{p,5}$, $\mathbf{q}_{p,6}$ are not affected by the movement of the external robot arm $\mathbf{q}_{p,1}$, $\mathbf{q}_{p,2}$, $\mathbf{q}_{p,3}$. The RMSE value are $[\mathbf{q}_{p,4}, \mathbf{q}_{p,5}, \mathbf{q}_{p,6}] = [0.187, 0.193, 0.360]$ and $[0.175, 0.207, 0.347]$ (rad) before and after fixing the external arm. **Bottom row:** Two wrist joint angles, $\mathbf{q}_{p,5}$ and $\mathbf{q}_{p,6}$, are closely coupled to each other. Joint \mathbf{q}_6 moved in correspondence to $\mathbf{q}_{p,5}$ despite its desired command was fixed as constant, and vice versa.

V. EXPERIMENTS

We evaluate the performance of the proposed methods on a physical dVRK robot [10]. The dVRK consists of two cable-driven, 7-DOF arms called patient-side manipulators (PSMs) that can be teleoperated by operating master tool manipulator arms (MTMs) or commanded programmatically. We use the Zivid OnePlus RGBD camera to track the position of the spheres on the arm and end effector, which can provide 1920x1200 pixel images at 13 frames per second with depth resolution 0.5 mm.

A. Modeling Approaches

In this section, we consider 14 possible learned models to estimate the ground-truth joint position and end-effector pose of the arm. We collect a large dataset of random motions and pick-and-place motions as described in Section IV-C. We also generate similar but smaller datasets as a validation set. All models are implemented in PyTorch [18] and trained using the MSE loss function and predict the three wrist joint angles $\hat{\mathbf{q}}_{p,4:6}^{(t)}$. The first three joints are not predicted or used as input, as we find they are very accurate and decoupled from the wrist joints as discussed in Fig. 6 and Section IV-D (thus in the notation below, it should be understood that \mathbf{q} refers to only the last 3 components of the robot's configuration).

We compute pose error by computing the forward kinematics of the arm using the new joint estimate.

We investigate the following modeling choices for the forward model f_θ :

1) *Architecture:* We consider the following candidate architectures for f_θ :

Linear: A linear regression from input to output using ℓ_1 regularization.

FF: A feed-forward neural network with two hidden layers, with each hidden layer having 256 units.

RNN: An LSTM [7] with 256 units, followed by a feed-forward neural network with two hidden layers of 256 units. Recurrent neural networks such as LSTMs

maintain a hidden state, which we hypothesize may better capture history dependent errors.

2) *Input Format:* To capture the history-dependent nature of cabling effects, we track a history of horizon $H > 1$ and use it to form two possible input formats:

Cmd: (\mathbf{x}_c) is the prior commanded joint positions.

Est: (\mathbf{x}_e) is the prior predictions and current desired joint position.

Thus, the input takes one of the following forms:

$$\mathbf{x}_c = \begin{bmatrix} \mathbf{q}_c^{(t)} \\ \mathbf{q}_c^{(t-1)} \\ \vdots \\ \mathbf{q}_c^{(t-H)} \end{bmatrix}, \quad \mathbf{x}_e = \begin{bmatrix} \mathbf{q}_c^{(t)} \\ \hat{\mathbf{q}}_p^{(t-1)} \\ \vdots \\ \hat{\mathbf{q}}_p^{(t-H)} \end{bmatrix}. \quad (\text{V.1})$$

We use \mathbf{x}_t to denote an input in one of these forms. At training time, we use ground truth $\mathbf{q}_p^{(t)}$ in place of the estimate $\hat{\mathbf{q}}_p^{(t)}$ to avoid compounding errors due to the model.

For the LSTM, each element of \mathbf{x}_t is supplied individually in a sequence.

3) *Output Format:*

Abs: $\hat{\mathbf{q}}_p^{(t)} = f_\theta(\mathbf{x}_t)$: the model directly predicts the absolute joint angles

Delta: $\hat{\mathbf{q}}_p^{(t)} = f_\theta(\mathbf{x}_t) + \mathbf{q}_c^{(t)}$: the model predicts the error of the robot's estimate.

For the inverse model g_ϕ , we perform the same search where $\mathbf{q}_c^{(t)}$ is replaced by $\mathbf{q}_p^{(t)}$ in the input and the model predicts $\hat{\mathbf{q}}_c^{(t)}$. Because $\mathbf{q}_p^{(t)}$ is not predicted by this model, we only use the \mathbf{x}_c input format.

For the linear model, we use a LASSO linear regression [30]. We observe the least-squares without regularization often overfits to the training data, while LASSO produces more stable results.

B. Offline Positioning Performance

We ablate all forward models in Section V-A offline with respect to H (Fig. 7) and find that most models' validation

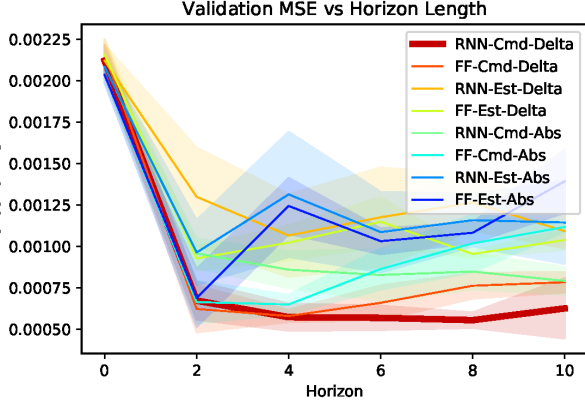


Fig. 7: **Forward Model Horizon Ablation** In this experiment, we ablate the input horizon H with respect to the models in Section V-A on $\mathcal{D}_{\text{pick}}$. We observe that the RNN model with the command as the input and predicted error as the output outperforms the other models, and roughly converges in performance around a horizon of 4. We observe that all models improve with a nonzero horizon, which implies that temporal information is necessary to compensate for hysteresis, cable stretch, and backlash. We train each model 5 times and report the mean and standard deviation.

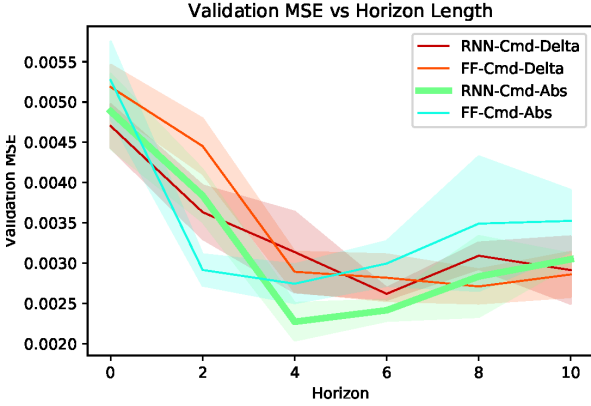


Fig. 8: **Inverse Model Horizon Ablation** We ablate the input horizon H with respect to the inverse versions of the models in Section V-A on $\mathcal{D}_{\text{pick}}$. We observe convergence in performance around a horizon of 4 using an RNN model with the command as the input and predicted joint angles as the output. We train each model 5 times and report the mean and standard deviation.

MSE start to converge around $H = 2$, which suggests that some temporal information is necessary to compensate for cabling effects. We also ablate all inverse models considered in Section V-A with respect to H on $\mathcal{D}_{\text{pick}}$ and find that the model 5 has the smallest validation MSE at $H = 4$ (Fig. 8). Based on these results, we select model RNN-Cmd-Delta as the best forward model design and model RNN-Cmd-Abs as the best inverse model design. Hereafter, we refer to these specific models when we refer to the forward and inverse models. To increase robustness, we use an ensemble of 10 of these models when designing controllers.

C. Trajectory Tracking Task

In this experiment, we evaluate the controller described in Section IV-F on a trajectory tracking task, where the objective is to guide the robot along a desired target trajectory $(\mathbf{q}_d^{(i)})_{i=0}^T$. We evaluate the performance of various controllers on a sequence of unseen pick and place trajectories. The

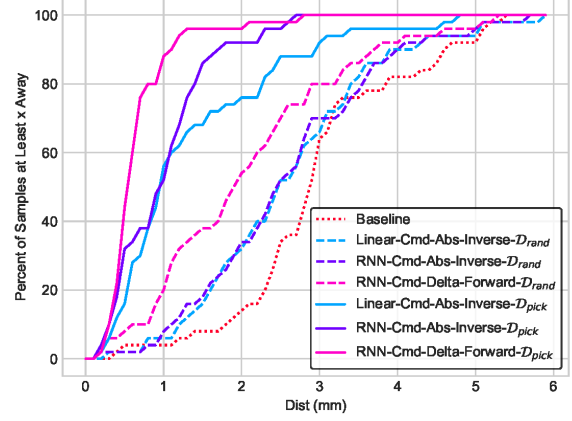


Fig. 9: **Cumulative Geometric Probability for Pick and Place Accuracy** Without the model, the end effector reaches within 1mm of the desired physical location for only 4.0% of pickups, while when using the model for correction, the robot ends within 1mm desired location 87.8% of the time. For 2 mm, this increases from 14.1% to 95.9%.

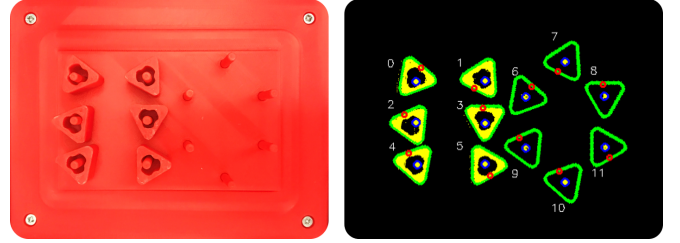


Fig. 10: Blocks, pegs, and peg board are monochrome (3D-printed red) to simulate a surgical setting. Blocks are detected using only depth information. The detected blocks are colored yellow and bordered green. Grasping points are displayed red.

controllers are trained on either $\mathcal{D}_{\text{rand}}$ or $\mathcal{D}_{\text{pick}}$ to measure the effect of distributional mismatch between the training data and target trajectories. For the forward model, we use $\alpha = 0.5$ and $M = 3$. Because we only calibrate the wrist joints, we evaluate using ground-truth information for $\mathbf{q}_{p,1:3}$. We find that the corrective model is able to reduce the mean tracking error of the physical robot from 2.96 mm to 1.90 mm training on $\mathcal{D}_{\text{rand}}$, and to 0.65 mm training on $\mathcal{D}_{\text{pick}}$ (Table I).

D. FLS Peg Transfer Task

We evaluate the proposed approach on a variant of the Fundamentals of Laparoscopic Surgery peg transfer task, which involves transferring 6 blocks from the left pegs to the right pegs in a peg board and then transferring them back (Fig. 10). The original task involves handing the block over between the two arms before placement onto the target peg, which we do not consider in this work. For consistency, we use monochrome setup as the six-block task from Hwang et al. [9], except we make several changes. We do not paint a peg board red, but instead make a 3D printing of the peg transfer which is colored red. This avoids an issue with sticky pegs which decreased performance in [9]. In addition, we also install springs at the bottom of the board to avoid potential hardware damage to the dVRK. We evaluate the uncalibrated robot, forward model controller, inverse model controller, and linear inverse model controller on this task. We find that without

TABLE I: **Physical pick and place accuracy:** We compare 3 different controller designs on $\mathcal{D}_{\text{rand}}$ and $\mathcal{D}_{\text{pick}}$, and evaluate their accuracy on a sequence of previously unseen test pick and place motions on the dVRK. We observe that the forward model-based controller is the most accurate on average, and the inverse model is slightly worse. Results suggest the mean tracking error is minimized by training on trajectories that are similar to those executed during the task.

Cartesian Distances (mm)	Uncalibrated	Linear Inverse		RNN Inverse		RNN Forward	
Training Dataset	—	$\mathcal{D}_{\text{rand}}$	$\mathcal{D}_{\text{pick}}$	$\mathcal{D}_{\text{rand}}$	$\mathcal{D}_{\text{pick}}$	$\mathcal{D}_{\text{rand}}$	$\mathcal{D}_{\text{pick}}$
Max	6.20	5.90	4.74	5.68	2.61	5.29	2.79
Min	0.51	0.21	0.20	0.13	0.11	0.11	0.18
Mean	2.96	2.58	1.34	2.57	0.97	2.05	0.65
Median	2.89	2.48	0.95	2.47	0.92	1.90	0.55
Standard deviation	1.19	1.14	1.05	1.15	0.60	1.21	0.44

TABLE II: **Peg Transfer Experiments:** We evaluate the learned controllers on 10 trials of the handover-free FLS peg transfer task. We observe that the baseline successfully transfers the block in 39.4 % of its attempts, but the forward model trained on random trajectory data is able to successfully transfer the block in 69.2 % of its attempts. The forward model trained on task-specific insertion data is able to complete 96.7 % of attempted transfers. Because the task involves transferring 6 blocks to the other side and transferring them back, each block is transferred twice. Blocks whose first transfer is unsuccessful cannot be transferred again, so trials that fail in the first half of the task may have less than 12 block transfer attempts. We observe that task-specific forward model never makes an error in the first wave.

Model	Dataset	Mean Transfer Time (s)	Pick Failure	Stuck	Fall	Success / Attempts	Success Rate
Baseline	—	10.0	90	3	10	67/170	0.394
RNN Forward	$\mathcal{D}_{\text{rand}}$	12.9	58	1	6	146/211	0.692
RNN Forward	$\mathcal{D}_{\text{pick}}$	13.6	0	2	6	232/240	0.967

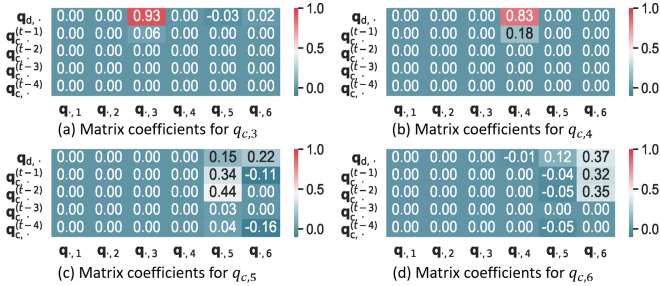


Fig. 11: View of the A matrix from linear regression. Each plot shows a single row of A reorganized to visualize the command and history effects on output command, with the target command in the first row, and the history of commands in subsequent rows. Rows of A for joints \mathbf{q}_1 and \mathbf{q}_2 are not included as they contain a single 1.0 in mapping $\mathbf{q}_{d,·}$ to $\mathbf{q}_{c,·}$ similar to the 0.93 for \mathbf{q}_3 in (a). Joints \mathbf{q}_4 (b), \mathbf{q}_5 (c), \mathbf{q}_6 (d) experience hysteresis which is observable by the effect previous commands on the output. Joints \mathbf{q}_5 (c) and \mathbf{q}_6 (d) are coupled, shown by their effects on each other.

calibration, the robot is only able to succeed at individual transfers 39.4 % of the time. With calibration on random trajectory data, the robot is able to succeed 69.2 % of the time. With calibration on pick and place data, the robot is able to succeed 96.7 % of the time. This is promising that using calibration, the resulting success rate is equivalent to performance by an expert human surgical resident 95.8 % [9]. This also suggests that the calibration procedure is effective, and closely matching the distribution of trajectories used for training with the distribution encountered at test time can yield better compensation (Table II).

E. Linear Regression Analysis

To gain insight into the cabling effects on joint coupling and hysteresis, we inspect the linear regression model. This model takes the form $g_{\text{lin}}(\mathbf{x}_t) = \mathbf{A}\mathbf{x}_t + \mathbf{b}$. Fig. 11 shows the values in A from a LASSO regression on a training dataset. From the matrix we observe that joints 1, 2, and 3 depend only on the target angle for that joint and not on an other command or history. Joint 4 exhibits some hysteresis as $\mathbf{q}_{c,4}$ is

function of both the $\mathbf{q}_{d,4}$ and the command history. Joints \mathbf{q}_5 and \mathbf{q}_6 exhibit both hysteresis and joint couplings as their \mathbf{q}_c is tied to the \mathbf{q}_d and the command history of both joints. The linear regression results match our observations, and suggest why a history-dependent models do better than baseline.

VI. CONCLUSION AND FUTURE WORK

We presented an efficient method for calibrating to the hysteresis and coupling effects of cable-driven surgical robots. The method tracks fiducial markers with an RGBD camera to build a dataset from which we learn a model. With a controller based on this model, we perform the FLS peg transfer task with a success rate that suggests that this method can improve precision over baseline.

In future work, we will apply the proposed calibration method to improve accuracy for other surgical tasks such as cutting, debridement, and peg transfer with hand-overs. One limitation of this work is that it requires a dataset of trajectories for a specific arm and instrument. To overcome this limitation, we will investigate the application of meta learning [3] to rapidly adapt to a new instrument or arm using a limited dataset by leveraging a large meta-training dataset generated from a set of arms and instruments. We will also investigate using the method to calibrate two PSM arms for multilateral surgical manipulation tasks.

ACKNOWLEDGEMENTS

This research was performed at the AUTOLAB at UC Berkeley in affiliation with the Berkeley AI Research (BAIR) Lab, Berkeley Deep Drive (BDD), the Real-Time Intelligent Secure Execution (RISE) Lab, the CITRIS “People and Robots” (CPAR) Initiative, and with UC Berkeley’s Center for Automation and Learning for Medical Robotics (Cal-MR). The authors were supported in part by donations from SRI International, Siemens, Google, Toyota Research Institute, Honda, Intel, and Intuitive Surgical. The da Vinci Research Kit was supported by the National Science Foundation, via the National Robotics Initiative (NRI), as part of the collaborative research project “Software Framework for Research in Semi-Autonomous

Teleoperation” between The Johns Hopkins University (IIS 1637789), Worcester Polytechnic Institute (IIS 1637759), and the University of Washington (IIS 1637444). Daniel Seita is supported by a National Physical Science Consortium Fellowship.

REFERENCES

- [1] G. Bradski, “The OpenCV Library,” *Dr. Dobbs’s Journal of Software Tools*, 2000.
- [2] C. D’Ettorre, G. Dwyer, X. Du, F. Chadebecq, F. Vasconcelos, E. De Momi, and D. Stoyanov, “Automated Pick-up of Suturing Needles for Robotic Surgical Assistance,” in *IEEE International Conference on Robotics and Automation (ICRA)*, 2018.
- [3] C. Finn, P. Abbeel, and S. Levine, “Model-Agnostic Meta-Learning for Fast Adaptation of Deep Networks,” in *International Conference on Machine Learning (ICML)*, 2017.
- [4] A. Garg, S. Sen, R. Kapadia, Y. Jen, S. McKinley, L. Miller, and K. Goldberg, “Tumor Localization using Automated Palpation with Gaussian Process Adaptive Sampling,” in *IEEE Conference on Automation Science and Engineering (CASE)*, 2016.
- [5] M. Haghighipanah, M. Miyasaka, Y. Li, and B. Hannaford, “Unscented Kalman Filter and 3D Vision to Improve Cable Driven Surgical Robot Joint Angle Estimation,” in *IEEE International Conference on Robotics and Automation (ICRA)*, 2016.
- [6] B. Hannaford, J. Rosen, D. Friedman, H. King, P. Roan, L. Cheng, D. Glozman, J. Ma, S. Kosari, and L. White, “Raven-II: An Open Platform for Surgical Robotics Research,” in *IEEE Transactions on Biomedical Engineering*, 2013.
- [7] S. Hochreiter and J. Schmidhuber, “Long short-term memory,” *Neural Computation*, vol. 9, 1997.
- [8] M. Hwang and D.-S. Kwon, “K-FLEX: A flexible robotic platform for scar-free endoscopic surgery,” *The International Journal of Medical Robotics and Computer Assisted Surgery*, 2020.
- [9] M. Hwang, D. Seita, B. Thananjeyan, J. Ichnowski, S. Paradis, D. Fer, T. Low, and K. Goldberg, “Applying Depth-Sensing to Automated Surgical Manipulation with a da Vinci Robot,” in *International Symposium on Medical Robotics (ISMR)*, 2020.
- [10] P. Kazanzides, Z. Chen, A. Deguet, G. Fischer, R. Taylor, and S. DiMaio, “An Open-Source Research Kit for the da Vinci Surgical System,” in *IEEE International Conference on Robotics and Automation (ICRA)*, 2014.
- [11] B. Kehoe, G. Kahn, J. Mahler, J. Kim, A. Lee, A. Lee, K. Nakagawa, S. Patil, W. Boyd, P. Abbeel, and K. Goldberg, “Autonomous Multilateral Debridement with the Raven Surgical Robot,” in *IEEE International Conference on Robotics and Automation (ICRA)*, 2014.
- [12] H. Kim, M. Hwang, J. Kim, J. M. You, C.-S. Lim, and D.-S. Kwon, “Effect of backlash hysteresis of surgical tool bending joints on task performance in teleoperated flexible endoscopic robot,” *The International Journal of Medical Robotics and Computer Assisted Surgery*, vol. 16, no. 1, p. e2047, 2020.
- [13] J. Mahler, S. Krishnan, M. Laskey, S. Sen, A. Murali, B. Kehoe, S. Patil, J. Wang, M. Franklin, P. Abbeel, and K. Goldberg, “Learning Accurate Kinematic Control of Cable-Driven Surgical Robots Using Data Cleaning and Gaussian Process Regression,” in *IEEE Conference on Automation Science and Engineering (CASE)*, 2014.
- [14] S. McKinley, A. Garg, S. Sen, R. Kapadia, A. Murali, K. Nichols, S. Lim, S. Patil, P. Abbeel, A. M. Okamura, and K. Goldberg, “A Disposable Haptic Palpation Probe for Locating Subcutaneous Blood Vessels in Robot-Assisted Minimally Invasive Surgery,” in *IEEE Conference on Automation Science and Engineering (CASE)*, 2015.
- [15] M. Miyasaka, J. Matheson, A. Lewis, and B. Hannaford, “Measurement of the Cable-Pulley Coulomb and Viscous Friction for a Cable-Driven Surgical Robotic System,” in *IEEE/RSJ International Conference on Intelligent Robots and Systems (IROS)*, 2015.
- [16] A. Murali, S. Sen, B. Kehoe, A. Garg, S. McFarland, S. Patil, W. D. Boyd, S. Lim, P. Abbeel, and K. Goldberg, “Learning by Observation for Surgical Subtasks: Multilateral Cutting of 3D Viscoelastic and 2D Orthotropic Tissue Phantoms,” in *IEEE International Conference on Robotics and Automation (ICRA)*, 2015.
- [17] P. Pastor, M. Kalakrishnan, J. Binney, J. Kelly, L. Righetti, G. Sukhatme, and S. Schaal, “Learning Task Error Models for Manipulation,” in *IEEE International Conference on Robotics and Automation (ICRA)*, 2013.
- [18] A. Paszke, S. Gross, F. Massa, A. Lerer, J. Bradbury, G. Chanan, T. Killeen, Z. Lin, N. Gimelshein, L. Antiga, A. Desmaison, A. Kopf, E. Yang, Z. DeVito, M. Raison, A. Tejani, S. Chilamkurthy, B. Steiner, L. Fang, J. Bai, and S. Chintala, “PyTorch: An Imperative Style, High-Performance Deep Learning Library,” in *Neural Information Processing Systems (NeurIPS)*, 2019.
- [19] S. A. Pedram, P. Ferguson, J. Ma, and E. D. J. Rosen, “Autonomous Suturing Via Surgical Robot: An Algorithm for Optimal Selection of Needle Diameter, Shape, and Path,” in *IEEE International Conference on Robotics and Automation (ICRA)*, 2017.
- [20] H. Peng, X. Yang, Y.-H. Su, and B. Hannaford, “Real-time Data Driven Precision Estimator for RAVEN-II Surgical Robot End Effector Position,” *arXiv:1910.06425*, 2019.
- [21] J. Rosen and J. Ma, “Autonomous Operation in Surgical Robotics,” *Mechanical Engineering*, vol. 137, no. 9, 2015.
- [22] H. Saeidi, H. N. D. Le, J. D. Opfermann, S. Leonard, A. Kim, M. H. Hsieh, J. U. Kang, and A. Krieger, “Autonomous Laparoscopic Robotic Suturing with a Novel Actuated Suturing Tool and 3D Endoscope,” in *IEEE International Conference on Robotics and Automation (ICRA)*, 2019.
- [23] J. Schulman, A. Gupta, S. Venkatesan, M. Tayson-Frederick, and P. Abbeel, “A Case Study of Trajectory Transfer Through Non-Rigid Registration for a Simplified Suturing Scenario,” in *IEEE/RSJ International Conference on Intelligent Robots and Systems (IROS)*, 2013.
- [24] D. Seita, A. Ganapathi, R. Hoque, M. Hwang, E. Cen, A. K. Tanwani, A. Balakrishna, B. Thananjeyan, J. Ichnowski, N. Jamali, K. Yamane, S. Iba, J. Canny, and K. Goldberg, “Deep Imitation Learning of Sequential Fabric Smoothing Policies,” in *arXiv:1910.04854*, 2019.
- [25] D. Seita, S. Krishnan, R. Fox, S. McKinley, J. Canny, and K. Goldberg, “Fast and Reliable Autonomous Surgical Debridement with Cable-Driven Robots Using a Two-Phase Calibration Procedure,” in *IEEE International Conference on Robotics and Automation (ICRA)*, 2018.
- [26] S. Sen, A. Garg, D. V. Gealy, S. McKinley, Y. Jen, and K. Goldberg, “Automating Multiple-Throw Multilateral Surgical Suturing with a Mechanical Needle Guide and Sequential Convex Optimization,” in *IEEE International Conference on Robotics and Automation (ICRA)*, 2016.
- [27] C. Shin, P. W. Ferguson, S. A. Pedram, J. Ma, E. P. Dutson, and J. Rosen, “Autonomous Tissue Manipulation via Surgical Robot Using Learning Based Model Predictive Control,” in *IEEE International Conference on Robotics and Automation (ICRA)*, 2019.
- [28] P. Sundaresan, B. Thananjeyan, J. Chiu, D. Fer, and K. Goldberg, “Automated Extraction of Surgical Needles from Tissue Phantoms,” in *IEEE Conference on Automation Science and Engineering (CASE)*, 2019.
- [29] B. Thananjeyan, A. Garg, S. Krishnan, C. Chen, L. Miller, and K. Goldberg, “Multilateral Surgical Pattern Cutting in 2D Orthotropic Gauze with Deep Reinforcement Learning Policies for Tensioning,” in *IEEE International Conference on Robotics and Automation (ICRA)*, 2017.
- [30] R. Tibshirani, “Regression Shrinkage and Selection Via the Lasso,” *Journal Of The Royal Statistical Society, Series B*, vol. 58, 1994.
- [31] J. Van Den Berg, S. Miller, D. Duckworth, H. Hu, A. Wan, X. Fu, K. Goldberg, and P. Abbeel, “Superhuman Performance of Surgical Tasks by Robots using Iterative Learning from Human-Guided Demonstrations,” in *IEEE International Conference on Robotics and Automation (ICRA)*, 2010.
- [32] M. Yip and N. Das, “Robot Autonomy for Surgery,” *The Encyclopedia of Medical Robotics*, 2017.
- [33] F. Zhong, Y. Wang, Z. Wang, and Y.-H. Liu, “Dual-Arm Robotic Needle Insertion With Active Tissue Deformation for Autonomous Suturing,” in *IEEE Robotics and Automation Letters (RA-L)*, 2019.